Journal of
Materials Chemistry A

Accepted Manuscript

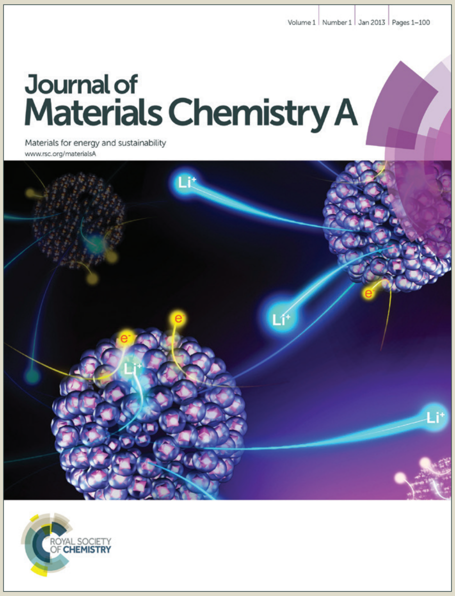

ROYAL SOCIETY
OF CHEMISTRY

www.rsc.org/materialsA

One-step in situ synthesis of ulthathin tungsten oxide@carbon nanowire webs as an anode material for high performance

Wenhui Zhang[a], Lu Yue*[a], Feng Zhang [a], Qinfang Zhang[a] Xuchun Gui[b] , Rongfeng Guan[a], Guihua Hou[a] and Ning Xu[a]

[a] *Key Laboratory for Advanced Technology in Environmental Protection of Jiangsu Province, Yancheng Institute of Technology, Jiangsu 224051, China*
[b] *State Key Lab of Optoelectronic Materials and Technologies, School of Physics and Engineering, Sun Yat-sen University, Guangzhou 510006, China*

Graphical abstract: Ulthathin $W_{18}O_{49}$@carbon nanowire web anode showed the best cycling performance (889 mAh g^{-1} after 250 cycles at 200 mA g^{-1}) for the tungsten oxide anode materials used in lithium-ion batteries reported to date.

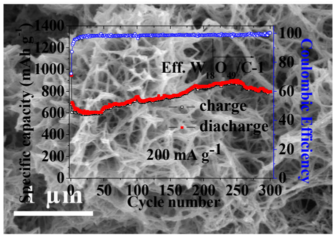

Cite this: DOI: 10.1039/c0xx00000x

www.rsc.org/xxxxxx

One-step in situ synthesis of ulthathin tungsten oxide@carbon nanowire webs as an anode material for high performance

Wenhui Zhang[a], Lu Yue*[a], Feng Zhang [a], Qinfang Zhang[a], Xuchun Gui[b] , Rongfeng Guan[a], Guihua Hou[a] and Ning Xu[a]

Received (in XXX, XXX) Xth XXXXXXXXX 20XX, Accepted Xth XXXXXXXXX 20XX
DOI: 10.1039/b000000x

A novel ulthathin $W_{18}O_{49}$@carbon nanowire web anode material for high performance lithium-ion batteries is synthesized via a facile one-step solvothermal method. Carbon layer is uniformly coated on ulthathin $W_{18}O_{49}$ nanowire bundles. The electrochemical properties are analyzed by cyclic voltammetry, galvanostatic charge/discharge cycling and electrochemical impedance. $W_{18}O_{49}$@carbon nanowire web electrode exhibits high lithium storage capacity of 889 mAh g^{-1} after 250 cycles at 200 mA g^{-1}, which is the best cycling performance for the tungsten oxide anode materials used in lithium-ion batteries reported to date. The improved electrochemical performance can be ascribed to the incorporation of carbon and the unique ulthathin nanowire web architecture of the nanocomposite.

1. Introduction

As an important semiconductor, tungsten oxide (WO_{3-x}) was used in a wide variety of applications such as gas sensors [1], photocatalysis [2], electrochromic devices [3], dye-sensitized solar cells [4], supercapacitors [5] and lithium-ion batteries [6, 7]. It also has been examined as an anode material for lithium-ion batteries due to its large theoretical capacity (693 mAh g^{-1}) than graphite (372 mAh g^{-1}), because the density of tungsten oxide (7.16 g cm^{-3}) is larger than that of graphite (2.26 g cm^{-3}), and the volumetric capacity of tungsten oxide is about four times that of graphite [8].

Recently, many efforts have been made to synthesize kinds of nanostructured tungsten oxide, such as hierarchical WO_3 flowers [6], mesoporous WO_3 [8], WO_3 nanorods [9], WO_3 nanowires [10], chrysanthemum-like $WO_3\cdot0.33H_2O$ [11], and WO_3 hollow nanospheres [12] for application in lithium-ion batteries. However, to date, the obtained specic capacitance/capacity, cycling stability and rate performance of previous tungsten oxide electrode materials have been still too low to meet the requirements of practical applications. It is very urgent to further improve their overall device performance. Nevertheless, as an anode material, tungsten oxide suffers from large structural and volume variation during the charge/discharge processes, and the induced structure change breaks the stability of electrode material, leading to mechanical disintegration and the loss of electrical connection between the active material and current collector, severely decreasing the cycling ability of electrodes. To overcome these problems, a practical and effective strategy is to create tungsten oxide composites by dispersing active nanoparticles in a lithium active/inactive matrix. Carbon has been extensively used as an active matrix due to its relatively low mass, good conductivity, small volume change, and reasonable lithium-insertion capacity. For example, L.N. Gao et al [13] reported WO_3 nanowire arrays/carbon cloth electrode exhibited a high capacity of 662 mAh g^{-1} after 140 cycles at a 0.28 C rate and excellent rate capabilities. M.P. Yu et al [14] reported WO_3 nanowires/graphene nanocomposite electrode exhibited a reversible lithium storage capacity of 656 mAh g^{-1} after 100 cycles at 100 mA g^{-1}.

Ultrathin 1D nanostructures including nanotubes and nanowires with ultrathin diameters less than 10 nm have attracted much research attention in the past few years owing to their unique chemical and physical properties [15-17]. Among various tungsten oxides, non-stoichiometric tungsten oxide of $W_{18}O_{49}$ is of great interest owing to the unusual defect structure and promising properties in the nanometer regime [18-21]. A.M. Cruz et al studied the electrochemical lithium insertion into $W_{18}O_{49}$, and thought that the maximum lithium content corresponded to $Li_{40}W_{18}O_{49}$ [22]. Up to now, however, the application of $W_{18}O_{49}$ in lithium-ion batteries as anode materials has been not reported.

In this work, we reported a novel ulthathin $W_{18}O_{49}$@carbon nanowire web anode material for high performance lithium-ion batteries which was synthesized by using a facile one-step solvothermal method. The first research work investigating ulthathin $W_{18}O_{49}$@carbon nanowire web led to promising electrochemical performance used as an anode material for high performance lithium-ion batteries.

2. Experimental

2.1 Preparation of $W_{18}O_{49}$/C composite

0.4 g WCl_6 and 0, 0.4 g or 0.8 g D-glucose were dissolved in 40 ml of triethylene glycol. The obtained solution was then transferred to a Teflon-lined stainless steel autoclave and heated at 200 °C for 5 h. The precipitate was collected, purified with distilled water, dried at 90 °C and then heat-treated at 450 °C for

2 h in Ar atmosphere. The obtained sample was named as $W_{18}O_{49}$, $W_{18}O_{49}$/C-1 and $W_{18}O_{49}$/C-2, respectively.

The obtained $W_{18}O_{49}$ sample and 0.4 g D-glucose were dissolved in 40 ml water. The obtained solution was then transferred to a Teflon-lined stainless steel autoclave and heated at 200 °C for 5 h. The precipitate was collected, purified with distilled water, dried at 90 °C and then heat-treated at 450 °C for 2 h in Ar atmosphere. The sample was named as $W_{18}O_{49}$/C-3.

2.2 Characterization of samples

The morphology of the samples was observed by a scanning electron microscope (SEM; Hitachi S-4800, Japan) with an energy dispersive spectroscopy (EDS) detector and transmission electron microscope (TEM; FEI Tecnai G2 Spirit, USA). The phase identification was performed by X-ray diffraction (XRD; PANalytical Empyrean, Netherlands) from 10° to 70°. The XPS spectra were obtained with ESCALAB250 XPS (Thermo Fisher Scientific, USA). The Brunauer-Emmett-Teller (BET) test was determined by an automated surface area and pore size analyzer (SI-MP-10/PoreMaster 33, Quanatachrome Instruments, US). Cyclic voltammetry (CV) and electrochemical impedance spectroscopy (EIS) results were obtained with Zennium/IM6 electrochemical workstation (Zahner, Germany).

2.3 Characterization of electrochemical performance

The coin cells (CR2025) were assembled to test the electrochemical performance of the as-prepared electrodes. The as-prepared samples were mixed with acetylene black and carboxymethyl cellulose, in a weight ratio of 60:20:20 in an aqueous solution to form homogeneous slurry. The slurry was spread onto a 10 µm thick copper foil and dried at 60 °C for 12 h in a vacuum oven and then pressed to obtain the electrode sheet with a 9-10 µm coating thickness and a loading level of about 1.4 mg cm^{-2}. The cells were assembled in an Ar filled glove-box, using 1 M $LiPF_6$ EC/DEC/DMC (1:1:1 by volume) as the electrolyte. The cells were charged and discharged galvanostatically in the fixed voltage window from 0.01 V to 3 V on a Shenzhen Neware battery cycler (China) at 25 °C.

EIS was measured by applying an alternating voltage of 5 mV over the frequency ranging from 10^{-2} to 10^5 Hz. In this work, unless otherwise specified, all impedance measurements were carried out after one cycle of the prepared electrode.

3. Results and discussion

The XRD patterns of the obtained samples are shown in Fig. 1a. It can be seen that all the patterns exhibited two intense diffraction peaks which corresponded to the [010] and [020] crystal faces of the monoclinic $W_{18}O_{49}$ structure (JCPDS card no. 71-2450). All the other diffraction peaks of samples were weak and broad. The XRD patterns strongly indicated that [010] was the possible crystal growth direction of the samples. In order to verify the valence of W element, XPS measurement was performed (Fig. S1), and the W4f-level spectrum of $W_{18}O_{49}$/C-1 was shown in Fig. 1b. This has been deconvuluted into six peaks indicating tungsten in multiple chemical states of W^{6+}, W^{5+} and W^{4+} as reported in some earlier studies [23, 24]. The percentages of W^{+6}, W^{5+} and W^{4+} state of $W_{18}O_{49}$/C-1 are 72.5%, 22.5% and 5.0%, respectively. This further confirms that the sample in $W_{18}O_{49}$ phase.

The morphologies of the samples were studied through SEM and TEM. Fig. 2(a-c) showed that $W_{18}O_{49}$ possessed urchin-like webs consisting of nanowires with a diameter about 20 nm. Interestingly, TEM images clearly revealed that the nanowires shown in Fig. 2(b-c) were composed of a lot of individual, thinner nanowires. The diameter of the thinner nanowires was only about 0.9 nm. Similar nanowire web morphology was observed for $W_{18}O_{49}$/C-1 (Fig. 2(d-f)), and a thin carbon layer with the thickness of about 0.6 nm was coated on the nanowire bundles. Fig. 2(g-i) showed that similar nanowire bundles with a thin carbon layer of about 0.6 nm thickness was observed for $W_{18}O_{49}$/C-2. Fig. 2(j-l) showed that the aggregation of nanowire bundles was observed for $W_{18}O_{49}$/C-3, and the thickness of carbon layer was about 4 nm.

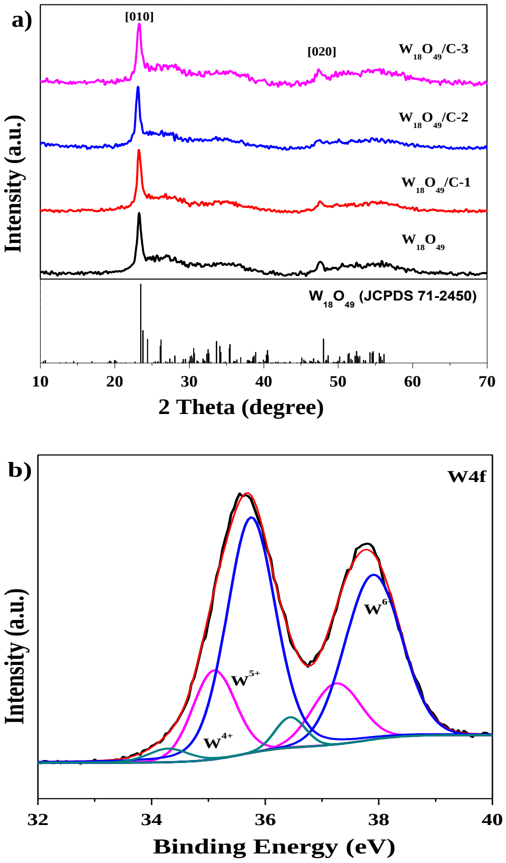

Fig. 1 a) XRD patterns of $W_{18}O_{49}$, $W_{18}O_{49}$/C-1, $W_{18}O_{49}$/C-2 and $W_{18}O_{49}$/C-3, b) W4f-level XPS spectrum of $W_{18}O_{49}$/C-1.

Further results of SEM examination of $W_{18}O_{49}$/C-1 combined with EDS mapping for the elements O, C and W are shown in Fig. 3. The bright regions corresponded to the presence of the elements O, C and W in Fig. 3b, c and d, respectively, indicating that O, C and W were distributed homogenously throughout the whole area. The C content of $W_{18}O_{49}$/C-1, $W_{18}O_{49}$/C-2 and $W_{18}O_{49}$/C-3 based on EDS analysis is shown in Table 1. The C content of $W_{18}O_{49}$/C-1, $W_{18}O_{49}$/C-2 and $W_{18}O_{49}$/C-3 was about 38.97%, 63.62% and 40.38% (at.%), respectively, indicating that the C content was consistent to the added content of D-glucose.

In order to investigate the electrochemical reaction mechanism, bare $W_{18}O_{49}$ and $W_{18}O_{49}$/C-1 anodes were characterized by XRD after charge and discharge. XRD patterns

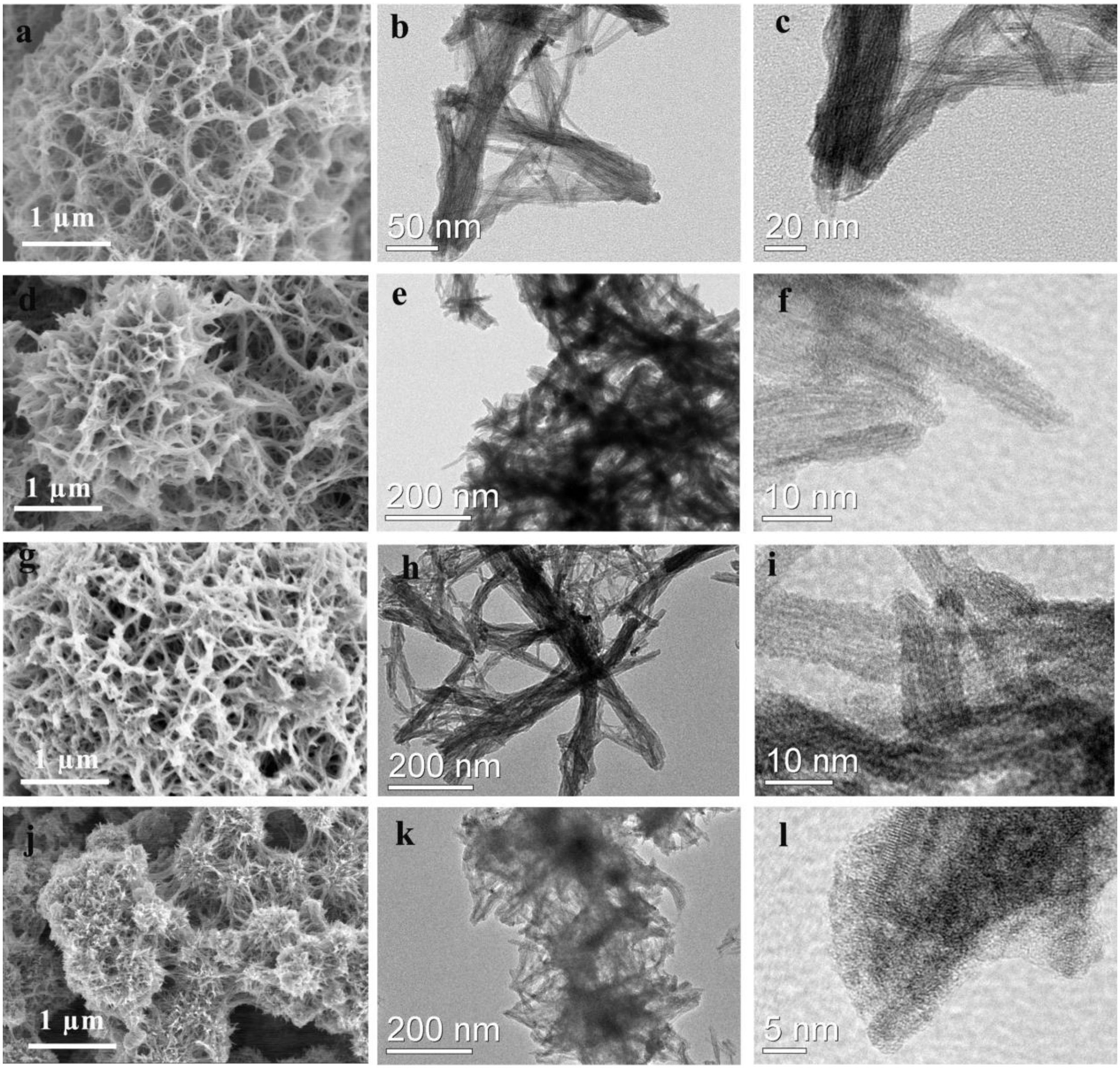

Fig. 2 (a) SEM and TEM images of (a-c) $W_{18}O_{49}$, (d-f) $W_{18}O_{49}$/C-1, (g-i) $W_{18}O_{49}$/C-2 and (j-l) $W_{18}O_{49}$/C-3.

of the $W_{18}O_{49}$ anode during lithium insertion/extraction of the second cycle are shown in Fig. 4. The peaks of Cu and C came from copper foil and conductive graphite, respectively [9]. The peak of 21° came from CMC [25]. After discharge, the diffraction peaks of about 10°, 19°, 23°, 30°, 42° and 47° could be indexed to $Li_xW_{18}O_{49}$ $(0 \leq x \leq 40)$ [22]. After charge, the diffraction peaks could be indexed to $W_{18}O_{49}$. XRD results demonstrated that the reversible electrochemical reaction between $W_{18}O_{49}$ and lithium could be expressed as follows:

$$W_{18}O_{49} + xLi^{+} + xe^{-} \longleftrightarrow Li_xW_{18}O_{49}\ (0 \leq x \leq 40) \quad (1)$$

CV of $W_{18}O_{49}$, $W_{18}O_{49}$/C-1 $W_{18}O_{49}$/C-2 and $W_{18}O_{49}$/C-3 electrodes was recorded between 0.01 V and 3.0 V, as is shown in Fig. 5. For the first cycle of bare $W_{18}O_{49}$ electrode, cathodic peaks were observed at about 1.5, 0.6 and 0.3 V, respectively, corresponding to the electro-chemical reduction reaction of $W_{18}O_{49}$ with lithium. However, during the following cycles, only one cathodic peak was noticed at about 0.8 V and all the other reduction peaks that appeared in the first cycle almost disappeared. In the anodic polarization of the first cycle, two oxidation peaks with maximum peaks at about 1.1 and 1.6 V were observed, which was associated with the lithium deinsertion processes [12, 14]. Apparently, the electrochemical reaction of $W_{18}O_{49}$ with lithium involved multi-steps for its decomposition and formation. The cathodic peak at 0.8 V and anodic peak at 1.1 V consisted of the main electrode reaction in lithium insertion and deinsertion processes as an oxidation-reduction couple. For the $W_{18}O_{49}$/C-1, $W_{18}O_{49}$/C-2 and $W_{18}O_{49}$/C-3 electrodes, there were basically consisted with $W_{18}O_{49}$ in CV curves. Nevertheless, besides the clear reduction peak in every cycle, both $W_{18}O_{49}$/C-1 and $W_{18}O_{49}$/C-3 electrodes displayed a higher peak current, indicating a better electrode reaction happened of that than $W_{18}O_{49}$ and $W_{18}O_{49}$/C-2 [26].

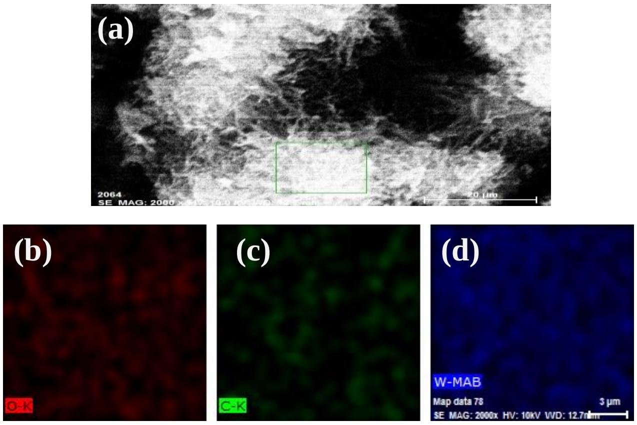

Fig. 3 Cross-sectional SEM image of $W_{18}O_{49}$/C-1 (a), with corresponding EDS mapping of O (b), (c) C and (d) W.

Table 1 C content of samples based on EDS analysis.

Sample	C norm. [wt.%]	C Atom. [at.%]
$W_{18}O_{49}$/C-1	10.87	38.97
$W_{18}O_{49}$/C-2	19.98	63.62
$W_{18}O_{49}$/C-3	14.21	40.38

The charge-discharge voltage profiles of $W_{18}O_{49}$, $W_{18}O_{49}$/C-1, $W_{18}O_{49}$/C-2 and $W_{18}O_{49}$/C-3 at a current density of 100 mA g^{-1} between 0.01 V and 3.0 V (vs. Li/Li^+) were displayed in Fig. 6. The open circuit voltage of these cells laid at about 3.1 V. During the first insertion process, an obvious discharge curve profile was observed for $W_{18}O_{49}$ electrode, due to the insertion of lithium ions into the $W_{18}O_{49}$ host. Electrochemical reactions of $W_{18}O_{49}$ with lithium involved multi-step for its decomposition and formation. There were three discharge voltage plateaus (1.5, 0.6 and 0.3 V) and two charge voltage plateaus (1.1 and 1.6 V) observed in the initial discharge and charge process, which agreed well with its CV curve profile. The highest discharge capacity of 1239 mAh g^{-1} was obtained in the first cycle, which is significantly higher than the tungsten oxide materials reported to date. However, the $W_{18}O_{49}$ electrode showed a low initial charge capacity of 543 mAh g^{-1} with a low initial coulomb efficiency of only 43.8%. The irreversible capacity could be assigned to the decomposition of electrolyte, forming a solid/electrolyte interphase on the electrode surface, and leading to the irreversible insertion of lithium ions into $W_{18}O_{49}$ host [27]. In the subsequent cycles, the discharging curves were different from the first discharge, while charging curves were identical with the first curve. The subsequent discharge curves became very smooth. As comparison, there were two non-obvious discharge voltage plateaus (0.7 and 0.3 V) observed in the initial discharge process for $W_{18}O_{49}$/C-1, $W_{18}O_{49}$/C-2 and $W_{18}O_{49}$/C-3 electrodes. They showed an improved initial coulomb efficiency of 66.8%, 70.8% and 59.5% due to the carbon layer protection, respectively. Specifically, the $W_{18}O_{49}$/C-1 electrode showed the best cycling performance, exhibiting the highest charge/discharge capacity of 731/745 mAh g^{-1} and 811/828 mAh g^{-1} at the 50th and 80th cycle, respectively.

The cycling performances of $W_{18}O_{49}$, $W_{18}O_{49}$/C-1, $W_{18}O_{49}$/C-2 and $W_{18}O_{49}$/C-3 at a current density of 100 mA g^{-1}

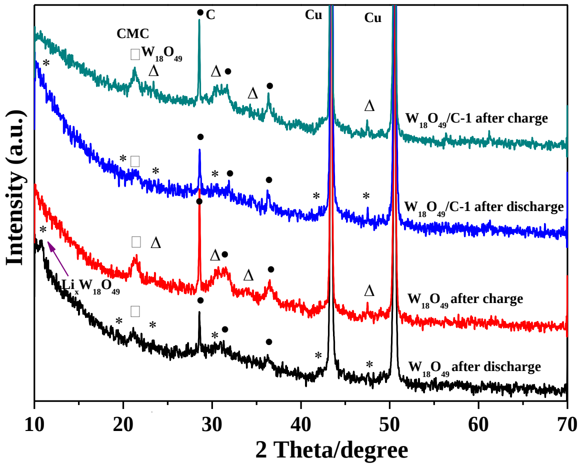

Fig. 4 XRD patterns of $W_{18}O_{49}$ and $W_{18}O_{49}$/C-1 anodes after charge and discharge.

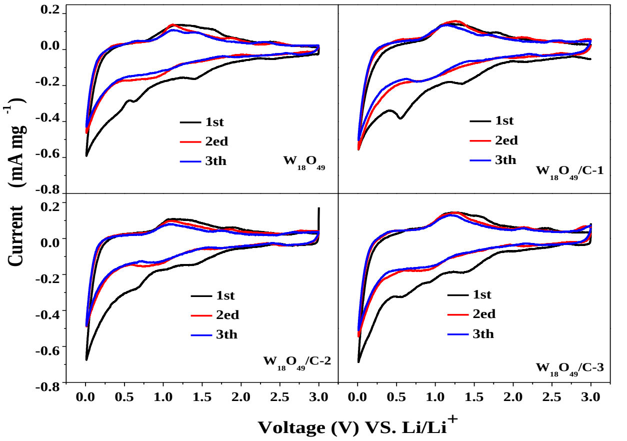

Fig. 5 Cyclic voltammograms of $W_{18}O_{49}$, $W_{18}O_{49}$/C-1, $W_{18}O_{49}$/C-2 and $W_{18}O_{49}$/C-3 in the voltage range of 0.01-3.0 V at a scan rate 0.5 mV s^{-1}.

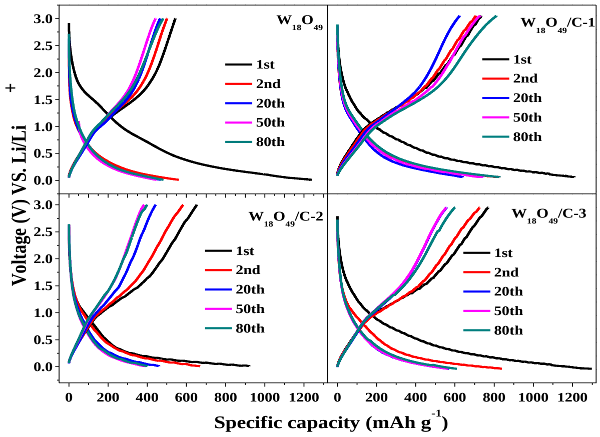

Fig. 6 Discharge-charge profiles of $W_{18}O_{49}$, $W_{18}O_{49}$/C-1, $W_{18}O_{49}$/C-2 and $W_{18}O_{49}$/C-3 at 100 mA g^{-1} in the voltage range of 0.01-3.0 V.

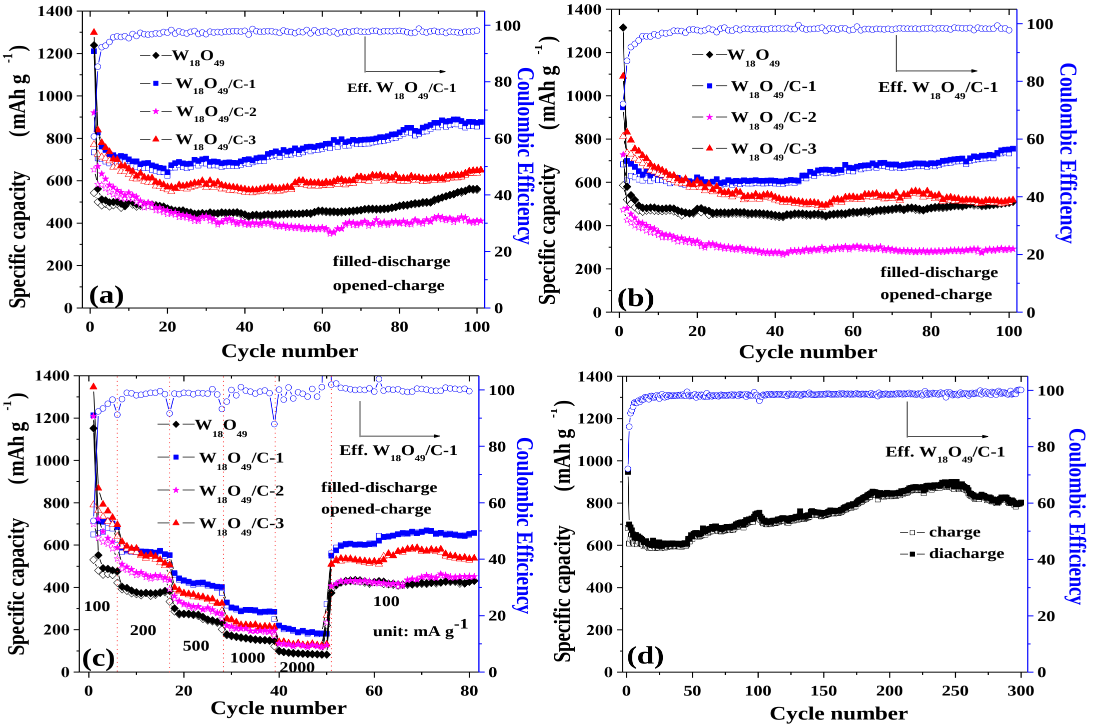

Fig. 7 Cycling stability of $W_{18}O_{49}$, $W_{18}O_{49}$/C-1, $W_{18}O_{49}$/C-2 and $W_{18}O_{49}$/C-3 at a rate of (a) 100 mA g^{-1}, (b) 200 mA g^{-1} and (c) rate performances; (d) Long-term cycling performance of $W_{18}O_{49}$/C-1 at a rate of 200 mA g^{-1}.

and 200 mA g^{-1} were displayed in Fig. 7(a/b). At 100 mA g^{-1}, the $W_{18}O_{49}$/C-1 electrode delivered a high initial charge/discharge capacity of 808/1210 mAh g^{-1} and exhibited a high average discharge capacity of 700 mAh g^{-1} for the first 40 cycles. Then, the capacity increased gradually and the discharge capacity of 872 mAh g^{-1} over 100 cycles was obtained, which was possibly attributed to some long-term activation process in the $W_{18}O_{49}$/C electrode during charge/discharge reactions [28, 29]. Compared with $W_{18}O_{49}$/C-1, $W_{18}O_{49}$/C-2 electrode delivered a lower initial charge/discharge capacity of 652/921 mAh g^{-1}, but a better coulombic efficiency of 70.8%. It was known that the carbon layer on the surface of oxide materials might sacrifice some lithium storage capacity, but also act as a protective layer to prevent the volume expansion and improve the electronic conductivity [30]. As a result, $W_{18}O_{49}$/C-2 electrode displayed an improved coulombic efficiency but delivered a lower capacity when compared with $W_{18}O_{49}$/C-1. The $W_{18}O_{49}$/C-3 electrode also delivered a high initial charge/discharge capacity of 770/1298 mAh g^{-1} with a coulombic efficiency of 59.3%. However, it exhibited a lower discharge capacity of 647 mAh g^{-1} over 100 cycles compared with $W_{18}O_{49}$/C-1. The capacity retention ratio of $W_{18}O_{49}$, $W_{18}O_{49}$/C-1, $W_{18}O_{49}$/C-2 and $W_{18}O_{49}$/C-3 electrode was 45.2, 72.1, 44.4 and 49.8% over 100 cycles, respectively. At 200 mA g^{-1}, the electrodes showed similar results. The $W_{18}O_{49}$/C-1 electrode displayed a better cycling performance, which delivered an initial charge/discharge capacity of 682/946 mAh g^{-1} with a coulombic efficiency of 72.1% and exhibited an increasing trend of the capacity after 45 cycles and the discharge capacity of 751 mAh g^{-1} over 100 cycles. The less content of C in the $W_{18}O_{49}$@C composite was also studied, as shown in Fig. S2. The results show that $W_{18}O_{49}$/C-1 exhibited the best cycling performance due to suitable carbon content. The rate capabilities of the electrodes are shown in Fig. 7c. The electrodes were cycled at a current density of 100 mA g^{-1} for the initial 6 cycles. Then the current density was increased gradually to 2000 mA g^{-1} and finally returned to 100 mA g^{-1}. The $W_{18}O_{49}$/C-1 electrode showed a first charge/discharge capacity of 649/1212 mAh g^{-1} with a coulombic efficiency of 53.5%. After 6 cycles, the coulombic efficiency was increased to 98%. At a higher current density of 200, 500, 1000 and 2000 mA g^{-1}, the capacity droped to about 392, 267, 163 and 92 mAh g^{-1} for $W_{18}O_{49}$ electrode, 472, 318, 208 and 131 mAh g^{-1} for $W_{18}O_{49}$/C-2 electrode and 560, 361, 229 and 136 mAh g^{-1} for $W_{18}O_{49}$/C-3 electrode, respectively. The long-term cycling performance and the coulombic efficiency of the $W_{18}O_{49}$/C-1 electrode at a current density of 200 mA g^{-1} are shown in Fig. 7d. The $W_{18}O_{49}$/C-1 electrode exhibited an increasing trend of the capacity after 45 cycles and the discharge capacity of 889 mAh g^{-1} over 250 cycles, and then stabilized to 801 mAh g^{-1} over 300 cycles. As far as we know, this is the best cycling performance for the tungsten oxide anode materials used in lithium-ion batteries reported to date.

To investigate the difference of electrochemical performance, EIS was employed to characterize the impedance properties of $W_{18}O_{49}$, $W_{18}O_{49}$/C-1 $W_{18}O_{49}$/C-2 and $W_{18}O_{49}$/C-3 electrodes. The Nyquist complex plane impedance plots of the electrodes after the first two charge–discharge cyclic processes were presented in Fig. 8. It can be seen that all the nyquist plots included two semicircle parts and one 45° linear diffusion drift for these electrodes. The 1st depressed semicircle at the high-frequency were contributed to the resistance of the interphase electronic contacts between the current collector and the solid electrolyte interface (SEI) film; the 2nd semicircle at the middle-frequency was due to the impedance of the charge transfer reaction at the interface of electrolyte and active material; the inclined line at the low frequency corresponded to the lithium ion diffusion process within the carbon electrodes [31, 32]. Based on the behavior of these EIS spectra and the aforementioned studies, a suggested equivalent circuit for the Nyquist plots of these electrodes was shown in Fig. 9(a) inset. This equivalent circuit was consisted of a series of four resistors elements, three constant phase elements (*CPE*) and a Warburg diffusion element. In the equivalent circuit, R_1 was composed of the electrolyte resistance (R_s) and the electrode resistance (R_e); R_2 represented the SEI film resistances; R_3 represented the interphase electronic contacts resistance; R_4 was the charge-transfer resistance across electrode/electrolyte interface; CPE_1 and CPE_2 was attributed by the lithium-ion diffusion in the SEI film and pore channel of the electrode materials, respectively; CPE_3 represented the electric double-layer capacitance of electrode/solution interface; the Z_W represented Warburg impedance was related to the semi-infinite diffusion of lithium ions into the bulk electrode [33].

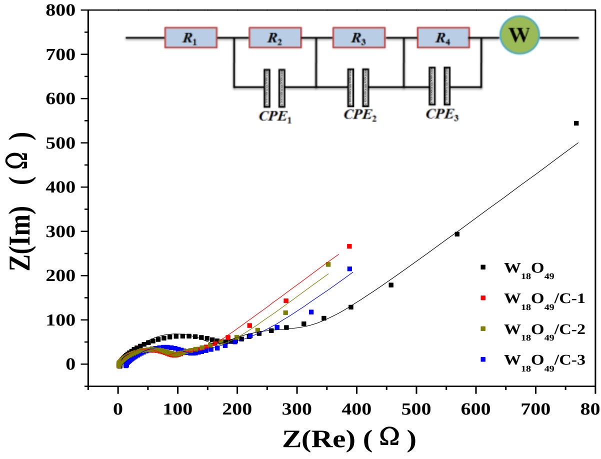

Fig. 8 Nyquist plots for $W_{18}O_{49}$, $W_{18}O_{49}$/C-1, $W_{18}O_{49}$/C-2 and $W_{18}O_{49}$/C-3 electrodes; the spots correspond to the experimental data, the solid lines stand for the calculated data. Equivalent circuit used to model the impedance spectra.

The fitted impedances (solid lines in Fig. 8) using the equivalent circuit agreed well with the actual impedance data. The corresponding parameters were obtained and summarized in Table 2. The resistance change of R_1 was similar for both $W_{18}O_{49}$ and $W_{18}O_{49}$/C composites. Compared to the $W_{18}O_{49}$ electrode, the decrease of R_2 in $W_{18}O_{49}$/C composites was observed. That is because a stable SEI film was formed after carbon coating, which decreased the resistance for lithium ion migration through the surface film [34]. The smaller R_3 was also observed in $W_{18}O_{49}$/C composites, which usually favored the fast transport of lithium ions and the electrons across the interface. It also indicated that the carbon layer supplied fast charge-transfer channels on the interface of $W_{18}O_{49}$ and electrolyte. The $Y_{0,\,1}$, $Y_{0,\,2}$ and $Y_{0,\,3}$ of the $W_{18}O_{49}$/C composite electrodes were higher than $W_{18}O_{49}$ electrode. The increase of $Y_{0,\,3}$ representing the electric double-layer capacitance favored the charge transfer for the electrode reaction. And the increase of $Y_{0,\,1}$ and $Y_{0,\,2}$ favored the diffusion of lithium ion in the SEI film and within the pore channels in the electrode, respectively [35, 36]. $W_{18}O_{49}$/C-1 electrode owned the least value of R_4, corresponding to the charge-transfer resistance in the electrode/electrolyte interface, which was about one-third and one-second of that for the $W_{18}O_{49}$ electrode and $W_{18}O_{49}$/C-3. Moreover, the value of $Y_{0.3}$ for $W_{18}O_{49}$/C-1 electrode was also the highest compared to other electrodes. Based on the above EIS analysis, $W_{18}O_{49}$/C-1 electrode exhibited favorable kinetic behavior, the lowest resistance and the highest capacitance, thus best cycling and rate performance among the tested samples. The impedance spectra of the $W_{18}O_{49}$/C-1 electrode in the delithiated state after different cycles are also shown in Fig. 9. With the increase of cycling, the semidiameter of the arc part decreased gradually in the Nyquist plots. It indicated that the cycles increased the activation grade in battery, which could improve the charge-transfer channels and reduce the residence on the interface of $W_{18}O_{49}$ and electrolyte. This phenomenon was consistent with the increase of capacity with cycling.

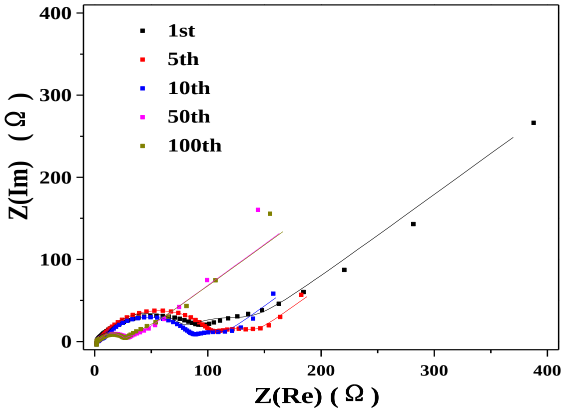

Fig.9 Nyquist plots for $W_{18}O_{49}$/C-1 electrode after 1, 5, 10, 50 and 100 cycles.

Eletrochemical properties of tungsten oxide and its composite with carbon by different processes are shown in Table 3. In can seen that ulthathin $W_{18}O_{49}$@carbon nanowire web anode material is the highest capacity value for the tungsten oxide and its composite with carbon used in lithium-ion batteries reported to date. The good cyclability of $W_{18}O_{49}$/C-1 could be ascribed to their homogenous carbon coated 1D and web-like nanostructures. Because carbon material coated on oxide particle surface could serve as a buffer layer to protect the inner active materials from huge volume changes, and significantly increase the electronic conductivity; the prepared nanostructured webs could improve the interconnectivity and increase the active sites on their surfaces; 1D nanostructures could accommodate the strain during lithium insertion/extraction and the pulverization of materials could be avoided.

The specific surface areas of $W_{18}O_{49}$, $W_{18}O_{49}$/C-1, $W_{18}O_{49}$/C-2 and $W_{18}O_{49}$/C-3 were examined by the BET method and were 61.8, 81.3, 60.1 and 59.4 m^2g^{-1}, respectively. Owing to the fact that a higher specific surface area increased the contact of the electrode and electrolyte, the $W_{18}O_{49}$/C-1 electrode was anticipated to show a better electrochemical property.

Table 2 Fitting parameters for the Nyquist plots in Fig. 8.

Sample I.D.	R_1 (Ω)	R_2 (Ω)	R_3 (Ω)	R_4 (Ω)	CPE_1		CPE_2		CPE_3	
					$Y_{0,1}$ (μF)	n	$Y_{0,2}$ (μF)	n	$Y_{0,3}$ (μF)	n
$W_{18}O_{49}$	3.88	18.15	117.20	112.70	2.50	1.07	5.93	0.96	130.00	0.80
$W_{18}O_{49}$/C-1	2.81	8.02	66.53	48.88	2.65	1.14	6.24	0.98	195.90	0.80
$W_{18}O_{49}$/C-2	2.85	8.31	76.99	75.05	2.56	1.13	7.03	0.95	171.70	0.76
$W_{18}O_{49}$/C-3	5.28	7.98	100.30	79.75	4.22	1.02	5.92	0.80	175.60	0.64

Y_0 and n are two parameters of the constant-phase element

Table 3 Eletrochemical properties of tungsten oxide and its composite with carbon by different processes.

The structure of material	Coulombic efficiency (%)	Specific discharge capacity (mAh g^{-1})	Rate capability (mAh g^{-1})	References
hierarchical WO_3 Flowers	~70.4	470 after 25 cycles at 50 mA g^{-1}	~450 (100 mA g^{-1}) ~350 (200 mA g^{-1}) ~250 (450 mA g^{-1}) ~150 (900 mA g^{-1})	[6]
WO_3 thin films	85.8	626 after 60 cycles at 0.02 $mAcm^{-2}$	/	[7]
mesoporous WO_3	/	~400 after 30 cycles at 0.2C	/	[8]
WO_3 nanorods	~72	607.2 after 30 cycles at 0.05C	/	[9]
chrysanthemum-like $WO_3{\cdot}0.33H_2O$	~85.2	370.7 after 20 cycles at 50 mA g^{-1}	~290 (100 mA g^{-1}) ~240 (150 mA g^{-1}) 215 (200 mA g^{-1})	[11]
WO_3 hollow nanospheres	74.0	294 after 100 cycles at 0.2C	~645 (200 mA g^{-1}) ~475 (400 mA g^{-1}) ~311 (1A g^{-1}) ~190 (2A g^{-1})	[12]
WO_3 nanowire arrays/carbon cloth	55	622 after 140 cycles at 0.28C	336 (1C) 132 (2C) 193 (3C) 108 (5C)	[13]
WO_3 nanowires/graphene	67.4	622 after 100 cycles at 100 mA g^{-1}	500 (200 mA g^{-1}) 360 (400 mA g^{-1}) 290 (800 mA g^{-1})	[14]
WO_3 nanowires	50	234 after 100 cycles at 100 mA g^{-1}	270 (200 mA g^{-1}) 220 (400 mA g^{-1}) 165 (800 mA g^{-1})	[14]
$W_{18}O_{49}$@carbon nanowire web	60.6	889 after 250 cycles at 200 mA g^{-1}	434 (500 mA g^{-1}) 306 (1 A g^{-1}) 200 (2 A g^{-1})	our work
$W_{18}O_{49}$	43.8	508 after 100 cycles at 200 mA g^{-1}	267 (500 mA g^{-1}) 163 (1 A g^{-1}) 92 (2 A g^{-1})	our work

(1C=693 mA g^{-1})

4. Conclusions

We reported a novel ulthathin $W_{18}O_{49}$@carbon nanowire web anode material for high performance lithium-ion batteries which was synthesized via a facile one-step solvothermal method. Carbon layer was uniformly coated on ulthathin $W_{18}O_{49}$ nanowires bundles. $W_{18}O_{49}$@carbon nanowire web electrode exhibited high reversible capacity of 889 mAh g^{-1} over 250 cycles at 200 mA g^{-1}, excellent cycling performance, remarkable rate capability and enhanced long-term cycling performance compared with the bare $W_{18}O_{49}$ nanowire electrode and $W_{18}O_{49}$@carbon nanowire web electrode prepared with two-step solvothermal/hydrothermal method. As far as we know, this is the best cycling performance for the tungsten oxide anode materials used in lithium-ion batteries reported to date.

Acknowledgements

This work was funded by the National Natural Science Foundation of China (No. 51402252, 21276220), the Natural Science Foundation of Jiangsu Province (No. BK20140463, BK20141262), National Key Technology R&D Program of China

(Grant no. 2013BAC13B01) and sponsored by Qing Lan Project.

Notes and References

[a] *Key Laboratory for Advanced Technology in Environmental Protection of Jiangsu Province, Yancheng Institute of Technology, Jiangsu 224051, China*
[b] *State Key Lab of Optoelectronic Materials and Technologies, School of Physics and Engineering, Sun Yat-sen University, Guangzhou 510006, China*

1. Y. S. Shim, L. Zhang, D. H. Kim, Y. H. Kim, Y. R. Choi, S. H. Nahm, C. Y. Kang, W. Lee and H. W. Jang, *Sensors And Actuators B-chemical*, 2014, **198**, 294-301.
2. G. C. Xi, Y. Yan, Q. Ma, J. F. Li, H. F. Yang, X. J. Lu and C. Wang, *Chemistry-a European Journal*, 2012, **18**, 13949-13953.
3. X. T. Chang, S. B. Sun, L. H. Dong, Y. H. Dong and Y. S. Yin, *Rsc Advances*, 2014, **4**, 8994-9002.
4. H. W. Zhou, Y. T. Shi, Q. S. Dong, Y. X. Wang, C. Zhu, L. Wang, N. Wang, Y. Wei, S. Y. Tao and T. L. Ma, *Journal of Materials Chemistry A*, 2014, **2**, 4347-4354.
5. Y. Y. Tian, S. Cong, W. M. Su, H. Y. Chen, Q. W. Li, F. X. Geng and Z. G. Zhao, *Nano Letters*, 2014, **14**, 2150-2156.
6. Y. C. Qiu, G. L. Xu, Q. Kuang, S. G. Sun and S. H. Yang, *Nano Research*, 2012, **5**, 826-832.
7. W. J. Li and Z. W. Fu, *Applied Surface Science*, 2010, **256**, 2447-2452.
8. S. Yoon, C. Jo, S. Y. Noh, C. W. Lee, J. H. Song and J. Lee, *Physical Chemistry Chemical Physics*, 2011, **13**, 11060-11066.
9. X. Y. Xue, B. He, S. Yuan, L. L. Xing, Z. H. Chen and C. H. Ma, *Nanotechnology*, 2011, **22**, 395702.
10. L. Meda, A. M. Dangerfield, M. C. Jones, C. M. White and A. Navulla, *Japanese Journal Of Applied Physics*, 2012, **51**, 11PE06.
11. J. Q. Yang, L. F. Jiao, Q. Q. Zhao, Q. H. Wang, H. Y. Gao, Q. N. Huan, W. J. Zheng, Y. J. Wang and H. T. Yuan, *Journal Of Materials Chemistry*, 2012, **22**, 3699-3701.
12. M. Sasidharan, N. Gunawardhana, M. Yoshio and K. Nakashima, *Nano Energy*, 2012, **1**, 503-508.
13. L. N. Gao, X. F. Wang, Z. Xie, W. F. Song, L. J. Wang, X. Wu, F. Y. Qu, D. Chen and G. Z. Shen, *Journal of Materials Chemistry A*, 2013, **1**, 7167-7173.
14. M. P. Yu, H. T. Sun, X. Sun, F. Y. Lu, T. Hu, G. K. Wang, H. Qiu and J. Lian, *Materials Letters*, 2013, **108**, 29-32.
15. W. H. Zhang, F. Wang and W. D. Zhang, *Dalton Transactions*, 2013, **42**, 4361-4364.
16. H. W. Lee, P. Muralidharan, R. Ruffo, C. M. Mari, Y. Cui and D. K. Kim, *Nano Letters*, 2010, **10**, 3852-3856.
17. C. H. Xu, J. Sun and L. Gao, *Nanoscale*, 2012, **4**, 5425-5430.
18. J. W. Liu, J. Zheng, J. L. Wang, J. Xu, H. H. Li and S. H. Yu, *Nano Letters*, 2013, **13**, 3589-3593.
19. G. C. Xi, S. X. Ouyang, P. Li, J. H. Ye, Q. Ma, N. Su, H. Bai and C. Wang, *Angewandte Chemie-international Edition*, 2012, **51**, 2395-2399.
20. D. Wang, J. Li, X. A. Cao, G. S. Pang and S. H. Feng, *Chemical Communications*, 2010, **46**, 7718-7720.
21. X. Q. Gao, F. Xiao, C. Yang, J. D. Wang and X. T. Su, *Journal of Materials Chemistry A*, 2013, **1**, 5831-5834.
22. A. M. Cruz, F. García-Alvarado, E. Morán, M. A. Alario-Franco and L. M. Torres-Martínez, *Journal of Materials Chemistry* 1995, **5**, 513-516.
23. L. Xiao, S. S. Zhang and J. H. Huang, *Powder Technology*, 2014, **258**, 297-303.
24. S. Sen, P. Kanitkar, A. Sharma, K. P. Muthe, A. Rath, S. K. Deshpande, M. Kaur, R. C. Aiyer, S. K. Gupta and J. V. Yakhmi, *Sensors And Actuators B-chemical*, 2010, **147**, 453-460.
25. H. L. Li, B. Wu, C. D. Mu and W. Lin, *Carbohydrate Polymers*, 2011, **84**, 881-886.
26. L. Yue, W. S. Li, F. Q. Sun, L. Z. Zhao and L. D. Xing, *Carbon*, 2010, **48**, 3079-3090.
27. Q. Si, K. Hanai, T. Ichikawa, A. Hirano, N. Imanishi, O. Yamamoto and Y. Takeda, *Journal of Power Sources*, 2011, **196**, 6982-6986.
28. H. Wu, N. Du, J. Z. Wang, H. Zhang and D. R. Yang, *Journal of Power Sources*, 2014, **246**, 198-203.
29. M. V. Reddy, G. V. S. Rao and B. V. R. Chowdari, *Chemical Reviews*, 2013, **113**, 5364-5457.
30. G. Wang, H. Wang, S. B. Cai, J. T. Bai, Z. Y. Ren and J. B. Bai, *Journal of Power Sources*, 2013, **239**, 37-44.
31. J. C. Guo, A. Sun, X. L. Chen, C. S. Wang and A. Manivannan, *Electrochimica Acta*, 2011, **56**, 3981-3987.
32. Z. Y. Zeng, J. P. Tu, X. L. Wang and X. B. Zhao, *Journal Of Electroanalytical Chemistry*, 2008, **616**, 7-13.
33. J. Y. Song, H. H. Lee, Y. Y. Wang and C. C. Wan, *Journal of Power Sources*, 2002, **111**, 255-267.
34. M. S. Wang and L. Z. Fan, *Journal of Power Sources*, 2013, **244**, 570-574.
35. L. Yue, S. Q. Wang, X. Y. Zhao and L. Z. Zhang, *Journal of Materials Chemistry*, 2012, **22**, 1094-1099.
36. L. Yue, W. H. Zhang, J. F. Yang and L. Z. Zhang, *Electrochimica Acta*, 2014, **125**, 206-217.